


Double-Gate Vectorial Frequency Control in Piezoresistive Nanowire Electromechanical Devices

Wataru Tomita,^{1,2} Satoshi Sasaki,¹ Motoki Asano¹,,¹ Kouta Tateno,¹ Hajime Okamoto,¹ and Hiroshi Yamaguchi^{1,*}

¹*NTT Basic Research Laboratories, NTT Corporation, Kanagawa 243-0198, Japan*

²*Department of Physics, Tohoku University, Miyagi 980-8578, Japan*

 (Received 17 November 2021; revised 14 March 2022; accepted 1 April 2022; published 21 April 2022)

Vacuum-gap and orthogonally aligned double-gate geometry is employed in a nanowire-based electromechanical resonator device to independently control two nearly degenerate orthogonal vibration modes. In the device, piezoresistance is the dominant mechanism of motion-induced conductance variation, which provides an efficient scheme for the self-transduction of vibrational motion into an electric signal. Two simultaneously applied gate voltages induce an opposite combined effect on the frequency shift between two vibration modes, which is well explained by model calculations. Using the opposite double-gate effect, we demonstrate vectorial control of two mode frequencies, which is not possible with single-gate geometry.

DOI: [10.1103/PhysRevApplied.17.044042](https://doi.org/10.1103/PhysRevApplied.17.044042)

I. INTRODUCTION

A semiconductor nanowire (NW), one of the most widely studied nanostructures, has great potential for application in high-performance electronic and optical devices [1]. NWs also play an important role in nanoelectromechanical systems (NEMSs), which functionalize the mechanical degrees of freedom of artificially fabricated three-dimensional nanostructures, in both classical and quantum domains [2,3]. NWs provide excellent performance, especially as a mechanical resonator [4–11], enabling us to integrate low-dimensional electronic systems to fabricate hybrid quantum devices [12–16]. NW-based mechanical resonators have two nearly degenerate flexural eigenmodes due to their symmetric cross-section shape [7–9,17–20]. The two diagonally vibrating modes are utilized in applications for nanomechanical resonators, such as vector sensors and scanning probe microscopes [21–23]. The ability to control these modes externally would make it possible to further functionalize NW-based mechanical devices.

In lithographically defined nanobeams, as well as in carbon nanotubes as nanomechanical elements, multiple-gate geometries are employed for fine and detailed control of both their electronic and mechanical properties [24–27]. The geometry allows the precise control of not only the specific electronic or mechanical states but also their mutual coupling. Especially, the independent

and detailed control of two nearly degenerate mechanical modes in semiconductor NWs is important in both fundamental physics and sensor applications [25,28–32].

Here, we fabricate a nanoelectromechanical resonator device using an InAs/InP core-shell NW with two orthogonal vacuum-gap gate electrodes and measure its fundamental mechanical resonance characteristics. We find that our core-shell NWs show large piezoresistivity with a resistance change on the order of more than 10^{-2} , in contrast to InAs NW devices, where the transconductance effect is dominant [7]. Efficient piezoresistive transduction allows us to detect vibrational modes at around 70 MHz without applying a large dc gate voltage. This dc-voltage-independent detection scheme enables detailed characterization of the frequency shift induced by the gate voltage. We observe a double-gate effect, where the two mode frequencies respond differently to the voltages simultaneously applied to the two gates. Numerical simulation clarifies that the electrostatic field distribution generated by the two gates implies the double-gate effect. Using these properties, we show that the double-gate geometry enables the separate modulation of the two resonance frequencies through vectorial voltage control, which is, so far, not enabled by the single-gate geometry.

II. EXPERIMENT

The nanoelectromechanical device consists of a doubly clamped suspended InAs/InP core-shell NW with a suspended length of 4 μm . Due to the employed growth process, the NW shape is tapered [33], with the diameter

*hiroshi.yamaguchi.zc@hco.ntt.co.jp

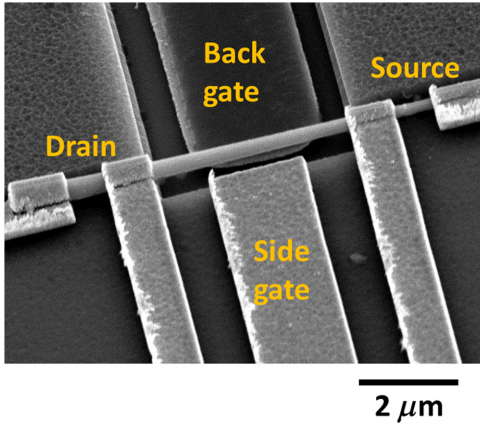


FIG. 1. Scanning-electron-microscope image of the fabricated nanowire NEMS device.

proportionally changing from 400 nm (at the left clamping point in Fig. 1) to 300 nm (at the right), as measured from the SEM observation. The nanowire has a cylindrical InAs core crystal covered by a 3-nm-thick InP shell, and two vacuum-gap gate electrodes are formed to control the mechanical motion. The back and side gates are separated from the NW by gaps of 250 and 600 nm, respectively. The NW also has source and drain Ohmic contacts that allow the detection of mechanical oscillation through conductance measurements. The gated transport characteristics indicate that the field effect is confirmed for both back and side gates [34]. A scanning-electron-microscope image of the fabricated device is shown in Fig. 1. We use inkjet printing to deposit a NW-dispersed liquid droplet, followed by indium whisker-assisted micromanipulation to align the NW on a patterned substrate [35]. The details of the fabrication process will be reported elsewhere.

The mechanical flexural motion of the NW is driven by applying an alternating electrostatic force through the gate electrodes. In our first series of experiments, we apply both dc and ac voltages to drive the flexural motion, following the procedure in previous reports [6–8,36,37]. In the case of a single-gate device, the electrostatic force applied to the grounded NW through the gate voltage $V_g(t) = V_{gdc} + V_{gac}\sqrt{2}\cos\omega_d t$, where V_{gac} is the modulation amplitude measured in the unit of root-mean-square (rms) voltage, is given by

$$\begin{aligned}
 F_d &= -\frac{1}{2} \left. \frac{\partial C(q)}{\partial q} \right|_{q=0} V_g(t)^2, \\
 &= -\left. \frac{\partial C(q)}{\partial q} \right|_{q=0} \left[\frac{V_{gdc}^2}{2} + \frac{V_{gac}^2}{2} + V_{gdc}V_{gac}\sqrt{2}\cos\omega_d t \right. \\
 &\quad \left. + \frac{V_{gac}^2 \cos 2\omega_d t}{2} \right], \tag{1}
 \end{aligned}$$

where q is the NW displacement measured from the equilibrium position, and $C(q)$ is the capacitance between the NW and gate electrode. When the drive frequency, $f_d = \omega_d/2\pi$, is around the resonance frequency, $f_0 = \omega_0/2\pi$ (referred to as “ f_0 drive” hereafter), the alternating force around the resonance frequency has an amplitude proportional to the voltage product $V_{gdc}V_{gac}$; therefore, both dc and ac voltages are required to induce the resonant motion. The motion is then detected through conductance variation by measuring the resistance change between the source and drain electrodes. To minimize the inductive crosstalk, we use a mixing technique [6–8,36–38], where an alternate source-drain bias voltage, $V_{SD}\sqrt{2}\cos(\omega_d + \Delta\omega)t$, is applied at a slightly detuned frequency from the drive voltage ($\Delta f = \Delta\omega/2\pi \sim 1.23$ kHz), and the current variation is detected at Δf by a lock-in amplifier. The setup is schematically shown in Fig. 2(a). The measurement is performed under vacuum ($<10^{-4}$ Pa) at cryogenic temperature (2–5 K).

III. FUNDAMENTAL RESONANCE AND TRANSDUCTION CHARACTERISTICS

Although both the back gate and side gate can drive the motion, we first examine the fundamental resonance and transduction characteristics of the NW by applying a voltage only to the back gate. Figure 3 shows the frequency response of current variation with various dc drive voltages. We observe two resonance peaks, one at around 66.7 and the other at 68.7 MHz, with quality factors (Q) in the range of 4000–4500, which correspond to the two orthogonal fundamental vibrational modes of the NW (hereafter referred as low- f and high- f modes, respectively). The resonance frequency of the tapered NW was already discussed in Ref. [33]. The mode wave function, $w(x)$, is given by the linear combination of Bessel functions:

$$w(x) = \frac{[AK_2(k_0\zeta) + BJ_2(k_0\zeta) + CY_2(k_0\zeta) + DI_2(k_0\zeta)]}{(l - \alpha x)}. \tag{2}$$

Here, J_2 and Y_2 are the first- and second-kind Bessel functions, and I_2 and K_2 are the first- and second-kind modified Bessel functions, with $\zeta = (2\sqrt{1 - \alpha x/l})/\alpha$. $l \sim 4 \mu\text{m}$ is the wire length and $\alpha = (a_0 - a_F)/a_0 \sim 0.25$ is the tapering parameter, where $a_0 \sim 200$ nm and $a_F \sim 150$ nm are the radii at the two clamping positions. k_0 is the normalized wave number, which is determined by applying the boundary condition of the doubly clamped beam structure:

$$w(0) = w(l) = 0, \quad w'(0) = w'(l) = 0, \tag{3}$$

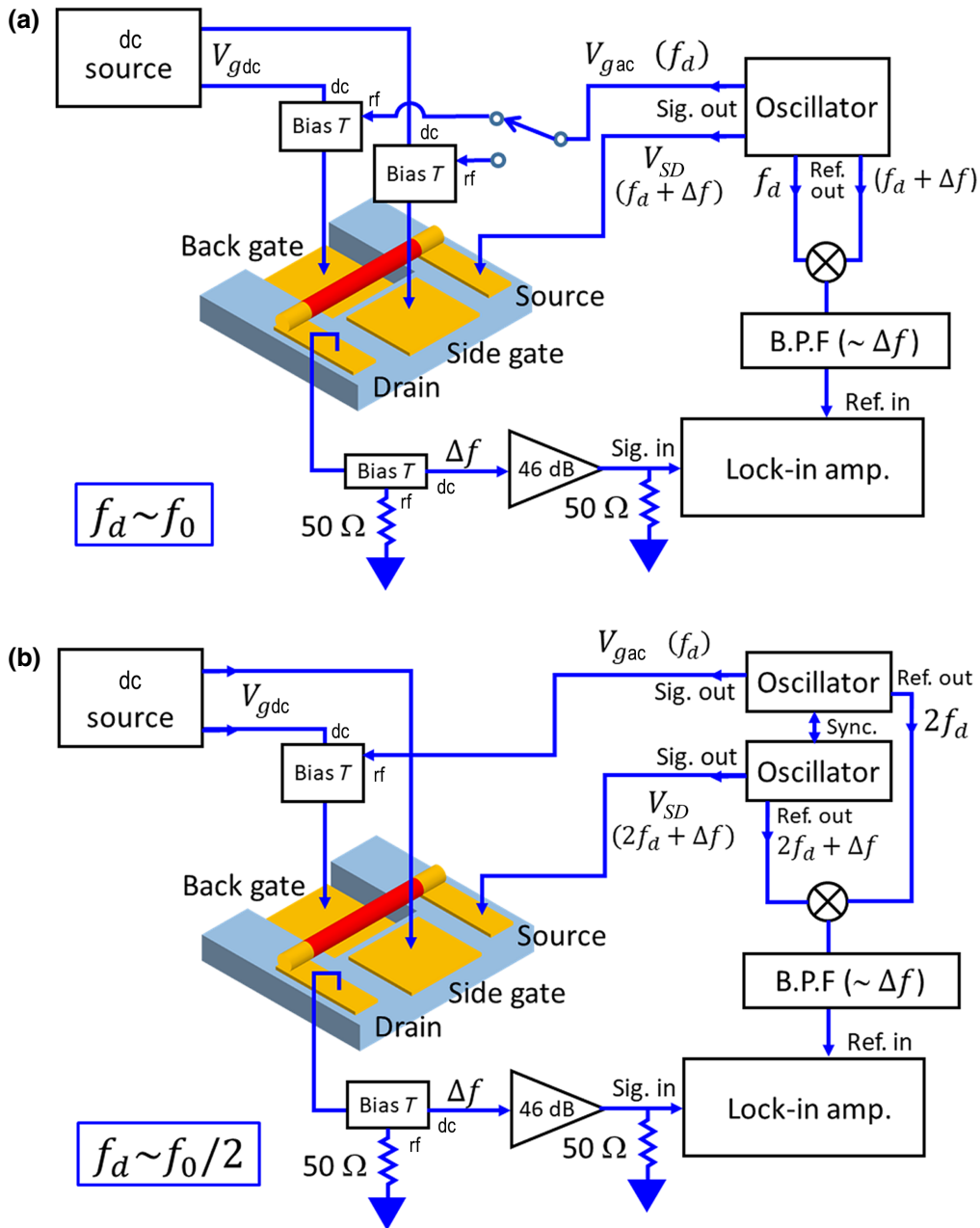


FIG. 2. (a) Experimental setup for the f_0 drive. Suspended NW is highlighted in red. (b) Setup used for $f_0/2$ -drive experiments. Unlike the f_0 drive (a), detection frequency is twice the drive frequency.

and is related to the resonance frequency, f_0 , by

$$f_0 = \omega_0/2\pi = \frac{k_0^2 a_0}{2\pi l^2} \sqrt{\frac{E}{4\rho}}, \quad (4)$$

where $E \sim 5.2 \times 10^{10}$ N/m² and $\rho \sim 5.7 \times 10^3$ kg/m³ are the Young's modulus and density of InAs, respectively. The numerical calculation gives $f_0 = 58.7$ MHz [33,34], which is about 12% lower than the average of the two observed frequencies. The origin of deviation is not known but could be the tension induced by the

fabrication and cooling processes. There are two degenerate fundamental modes corresponding to mechanical vibration in two orthogonal directions, and the observed splitting of about 2 MHz is caused by the noncylindrical shape of the NW cross section [7–9,13,17–19] and clamping.

In both modes, we observe a frequency redshift and an increased amplitude of peak-current variation with increasing V_{gdc} . Closed-triangle plots in Fig. 4(a) show the peak frequency as a function of V_{gdc} . The quadratic voltage dependence is consistent with the theoretical prediction

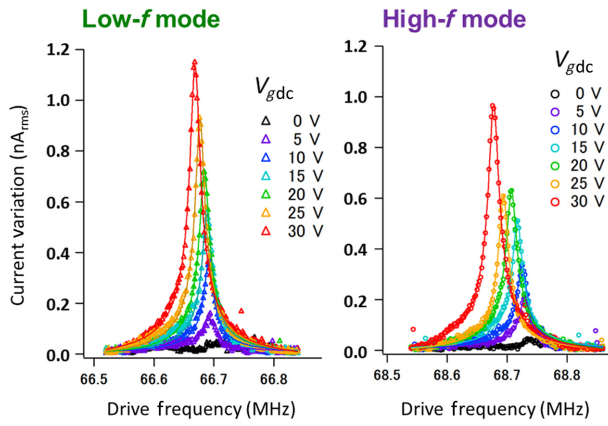


FIG. 3. Drive-frequency response of current variation with various dc gate voltages (V_{gdc}), measured under vacuum at 2.2 K. We use a source-drain voltage (V_{SD}) of 5 mV_{rms}. Lines show their Lorentzian fitting curves.

[39]; the frequency, $f(V_{gdc})$, is given by

$$f(V_{gdc}) = f_0 \left[1 - \frac{1}{4m\omega_0^2} \sum_{ij} \frac{\partial^2 C(q)}{\partial q^2} V_{gdc}^2 \right]_{q=0}, \quad (5)$$

where m is the effective mass of the resonance mode, and $C(q)$ is the capacitance between the NW and back gate as a function of nanowire displacement, q . Within the used voltage range ($|V_{gdc}| \leq 30$ V), we do not observe the tension-induced positive frequency shift reported in InAs NW devices [12], probably because the field effect in our device is much less than that in their devices.

A remarkable feature is observed in the gate-voltage dependence of signal amplitude [closed triangles in Fig. 4(b)]. The peak-current variation is proportional to V_{gdc} in both the low- f and high- f modes. It is reasonable to assume that the signal amplitude is proportional to both the driving force amplitude and detection efficiency. As already described in Eq. (1), the force amplitude in the electrostatic drive at around f_0 is proportional to $V_{gdc}V_{gac}$. This dependence is also experimentally confirmed by measuring the onset of Duffing bistability in our device [34]. Thus, the linear dependence of current variation with fixing V_{gac} suggests that the detection efficiency is independent of V_{gdc} .

Two detection mechanisms are reported in nanowire NEMS devices. One is the transconductance effect, which is caused by conductance variation through the capacitance modulation between the gate and NW [7,8,36,37]. The effect requires a nonzero gate voltage, and the conductance variation is proportional to V_{gdc} . The other is the piezoresistive effect [6], which is caused by the intrinsic material properties and is independent of V_{gdc} . The observed linear V_{gdc} dependence of the signal amplitude suggests that the piezoresistance is responsible for current modulation in our

device. This observation is contrary to that for InAs-based NW NEMS devices, where the transconductance effect is the dominant mechanism [7]. In addition, piezoresistive current modulation in a NW electromechanical device using other materials is observed not at the drive frequency but at the second-order harmonics, reflecting the symmetric cross-section shape [6]. This is also contrary to our system.

Then, we perform half-frequency-drive measurements to directly confirm that the detection efficiency is independent of V_{gdc} . The measurement setup is shown in Fig. 2(b). While detecting the conductance variation at around f_0 , we drive the mechanical motion at the half frequency, $f_d \sim f_0/2$ (referred to as “ $f_0/2$ drive” hereafter). From Eq. (5), the driving force at around the resonance frequency, $f_0 \sim 2f_d$, is given by

$$F_d \sim - \frac{\partial C(q)}{\partial q} \bigg|_{q=0} \left[\frac{V_{gac}^2 \cos 2\omega_d t}{2} \right]. \quad (6)$$

This driving force is independent of V_{gdc} ; thus, we can directly confirm that detection does not require the application of V_{gdc} .

Figure 5 shows the current-variation amplitude measured in the $f_0/2$ -drive experiments with different dc gate voltages. The measurement is performed using the modified experimental setup shown in Fig. 2(b). The mechanical resonance is clearly confirmed when the motion is driven at the half frequency in the $f_0/2$ -drive experiments.

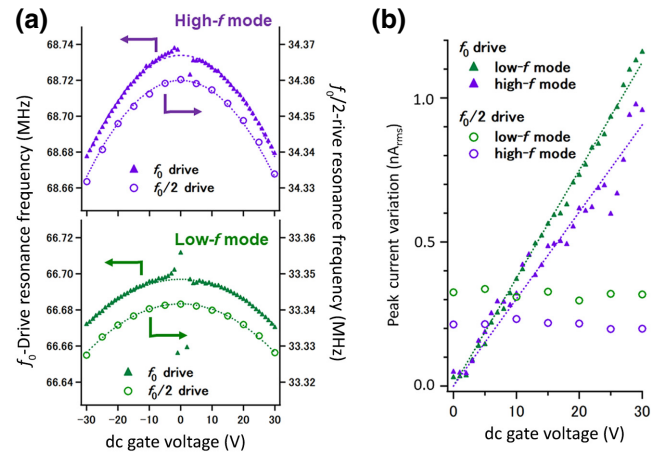


FIG. 4. (a) Resonance frequency obtained by Lorentzian fitting of measured resonance curves in f_0 -drive (closed triangles) and $f_0/2$ -drive (open circles) experiments. Dotted lines are their quadratic fitting curves. Constant-frequency difference observed between f_0 drive and $f_0/2$ drive is caused by a slow drift in the resonance frequency between two different series of experiments. (b) Peak-current variation obtained in f_0 -drive (closed triangles) and $f_0/2$ -drive (open circles) experiments. Dotted lines are linear fittings of the former. Source-drain voltages of 5 and 2 mV_{rms} are used for f_0 and $f_0/2$ drives, respectively.

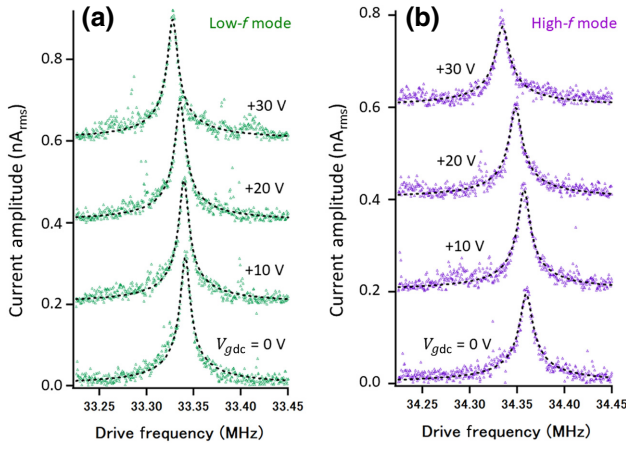


FIG. 5. Measured frequency response of current-variation amplitude in $f_0/2$ -drive experiments for (a) low- f mode and (b) high- f mode. Back-gate drive voltage of $5 V_{\text{rms}}$ and source-drain bias voltage of $2 \text{ mV}_{\text{rms}}$ are used, with a measurement temperature of 3.7 K . No visible change in peak amplitude is observed in response to dc gate-voltage (V_{gdc}) variation.

The peak amplitude is independent of the dc gate voltage, while the frequency redshift is again observed. More detailed plots of peak amplitude and resonance frequency are shown as a function of dc gate voltage by open circles in Figs. 4(a) and 4(b). They indicate that the peak-current amplitude is nearly constant, whereas the peak frequency quadratically depends on V_{gdc} in the same manner as the f_0 drive. (The constant-frequency difference observed between the f_0 drive and $f_0/2$ drive is not caused by the difference in drive method but by a slow drift in the resonance frequency between two different series of experiments.) From the $f_0/2$ -drive experiments, we can conclude that the driving force is proportional to the dc gate voltage, while the detection efficiency is independent of it. These results confirm that the piezoresistance is responsible for current modulation in our device.

Even if we assume that there is no reflection in the actuation rf line and the ac voltage of V_{SD} is fully applied to the device, which has a two-terminal dc resistance of $3.3 \text{ k}\Omega$, the current modulation ratio, $\Delta I_{SD}/I_{SD}$, at the bifurcation point is estimated to be in the order of up to 10^{-2} , in spite of the small piezoresistive coefficient of narrow-gap InAs. Furthermore, unlike in previous reports on piezoresistive detection, where the detection frequency is twice the vibration frequency [6], the detection frequency is identical to the vibration frequency in this study, showing the asymmetric piezoresistive response to the vibration direction. The InAs/InP core-shell structure is reported to have nonuniform strain distribution localized at the interface [40], and the Ohmic contact formed around the interface can play some role in inducing the asymmetric piezoresistive properties. While further comprehensive study is

required to clarify the detailed mechanism, the piezoresistive self-transduction scheme confirmed in this study generates a fundamental harmonic signal without the help of the dc gate voltage. This highly efficient means of motion detection will be useful in future sensor applications of NW NEMS devices.

IV. DOUBLE-GATE EXPERIMENTS AND FREQUENCY CONTROL OF TWO VIBRATIONAL MODES

The efficient piezoresistive self-transduction scheme together with the $f_0/2$ -drive technique allows the detailed and comprehensive characterization of the resonance frequency shift induced by simultaneously applying two gate voltages. Figure 6 shows the measured frequency as a function of side-gate and back-gate voltages. As in the case of single-back-gate experiments, the frequency shows a quadratic redshift as a function of side-gate voltage. An interesting feature is observed in the difference between the low- f and high- f modes when both gate voltages are applied. In the low- f mode, the two voltages show a constructive contribution, where a larger redshift is observed when the two voltages have the same sign than when they have the opposite one. In contrast, the contribution is destructive in the high- f mode, where the redshift becomes suppressed when the two voltages have the same sign. To understand the opposite double-gate response between the two modes, we perform a model calculation of the frequency shift.

For qualitative analysis, we use a three-wire-capacitor model, in which two wires correspond to the gate electrodes and one to the NW mechanical oscillator [Fig. 7(a)]. The effective lateral offset of the back-gate position, d_{offset} , is considered because the back-gate metal film is deposited

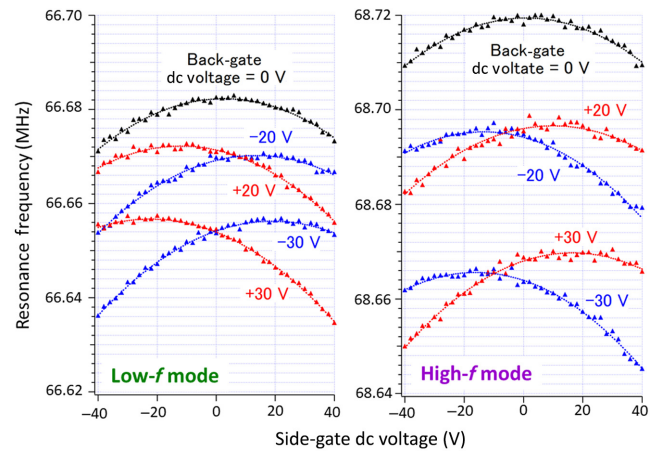


FIG. 6. Resonance frequency as a function of side-gate and back-gate voltages determined by $f_0/2$ -drive experiments. Back-gate drive voltage of $5 V_{\text{rms}}$ and source-drain bias voltage of $5 \text{ mV}_{\text{rms}}$ are used, with a measurement temperature of 5.0 K .

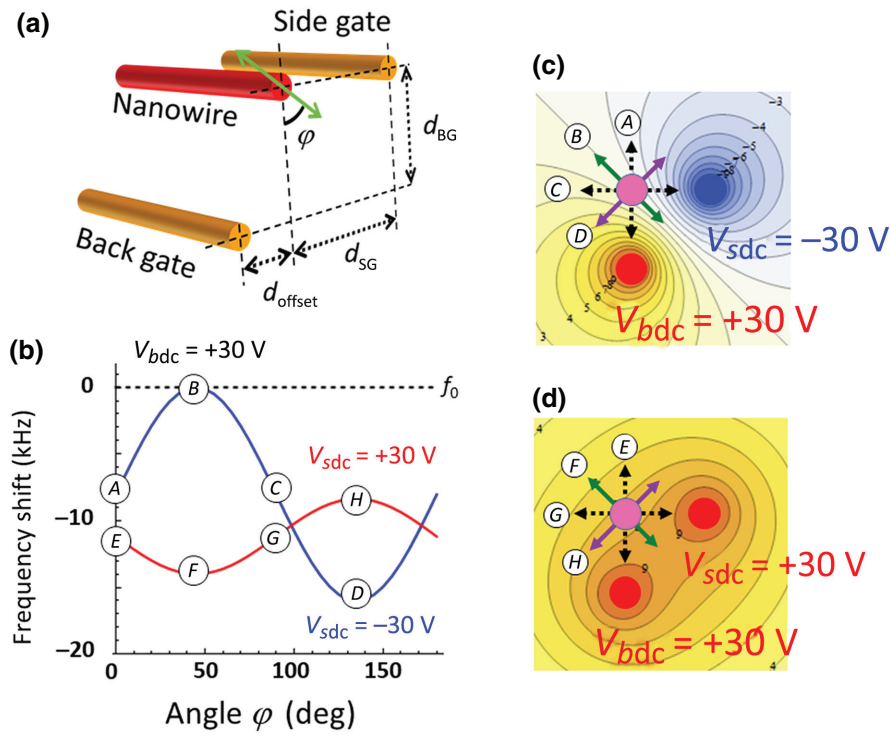


FIG. 7. (a) Schematic illustration of three-wire-capacitor model. Green arrow shows the mechanical vibration axis, which has a tilt angle of φ from the device surface normal. (b) Calculated shift in the resonance frequency induced by the dc back-gate voltage $V_{bdc} = +30$ V with two side-gate dc voltages, $V_{sdc} = +30$ V (red) and -30 V (blue), as a function of tilt angle φ . Circled letters (A–H) correspond to the vibration axis shown in (c),(d). Equipotential contour maps of electrostatic potential generated by the two gate electrodes, calculated by finite-element simulation for side-gate voltages (V_{sdc}) of (c) -30 V and (d) $+30$ V, both with $V_{bdc} = +30$ V. Comparison with experiments shows that low- f mode corresponds to the vibration axis shown by green arrows ($\varphi \sim 45^\circ$), whereas high- f mode corresponds to that shown by purple arrows ($\varphi \sim 135^\circ$).

only on the side opposite the side gate (see Fig. 1). The diameters of the nanowire and two gate wires are assumed to be uniform and identical (400 nm) for simplicity. When the voltage of each conductor is kept constant, the total potential energy as a function of eigenmode displacement, q , is effectively given by [41]

$$V(q) = \frac{m}{2} \omega_0^2 q^2 - \frac{l_{\text{eff}}}{2} \sum_{i,j=b,s} C_{ij}(q) V_{idc} V_{jdc}. \quad (7)$$

Here, m is the effective mass of the eigenmode with angular frequency ω_0 ; V_{idc} is the dc voltage applied to the back ($i = b$) and side ($i = s$) gates; l_{eff} is the effective length of the nanowire; and $C_{ij}(q)$ is the capacitance matrix per unit length, which is the inverse of the elastance matrix, $P_{ij}(q)$, approximately given by [34]

$$\begin{aligned} P_{ss}(q) &= \frac{1}{\pi \epsilon_0} \log \frac{D_{sN} + \sqrt{D_{sN}^2 - 4a^2}}{2a}, \\ P_{bb}(q) &= \frac{1}{\pi \epsilon_0} \log \frac{D_{bN} + \sqrt{D_{bN}^2 - 4a^2}}{2a}, \\ P_{sb}(q) &= P_{bs}(q) = \frac{1}{2\pi \epsilon_0} \log \\ &\quad \times \frac{(D_{bN} + \sqrt{D_{bN}^2 - 4a^2})(D_{sN} + \sqrt{D_{sN}^2 - 4a^2})}{2a(D_{bs} + \sqrt{D_{bs}^2 - 4a^2})}. \end{aligned} \quad (8)$$

Here, D_{lm} ($l, m = b, s, N$) is the dynamic distance between the two wires given by

$$\begin{aligned} D_{bs} &= \sqrt{(d_{\text{offset}} + d_{SG})^2 + d_{BG}^2}, \\ D_{bN} &= \sqrt{(d_{\text{offset}} - q \sin \varphi)^2 + (d_{BG} + q \cos \varphi)^2}, \\ D_{sN} &= d_{SG} + q \sin \varphi, \end{aligned} \quad (9)$$

where d_{SG} is the static (steady-state) distance between the NW and side gate, d_{BG} is the static vertical distance between back gate and NW, q is the NW displacement, and φ is the tilt angle (see Fig. 7).

Using the electrostatic potential, the shift in resonance frequency is calculated as a function of mode angle φ , as shown in Fig. 7(b). As the first simple example to confirm qualitative behavior, we use $d_{BG} = d_{SG} = 1 \mu\text{m}$ with $d_{\text{offset}} = 0$. We introduce the coupling strength, g , as a fitting parameter defined by

$$g \equiv \frac{\epsilon_0 l_{\text{eff}}}{8\pi m}, \quad (10)$$

and use the value $g = 0.002 \text{ MHz}^2 \text{ m}^2 \text{ V}^{-2}$, which reproduces a similar order of frequency shift (~ 10 kHz).

The simulation qualitatively reproduces the experiments; the two voltages have a constructive contribution when the angle, φ , is about 45° , whereas they have a destructive contribution when the angle, φ , is about 135° . The results can be well explained by considering

the electrostatic field distribution. Figures 7(c) and 7(d) schematically show the equipotential contour lines of electrostatic potential generated by the two cylindrical gate electrodes calculated by finite-element simulations. The $\varphi \sim 45^\circ$ vibration is along the equipotential surface when voltages with opposite signs are applied to the two gates [B in Fig. 7(c)] but perpendicular to the surface when voltages with the same sign are applied [F in Fig. 7(d)]. The opposite tendency is observed when the vibration is in the $\varphi \sim 135^\circ$ direction (D and H). Because the frequency shift is approximately given by the electric field gradient, the equipotential maps indicate that the two voltages have constructive and destructive contributions when the tilt angle, φ , is about 45° and 135° , which corresponds to the low- f and high- f modes, respectively.

The framework of the three-wire model can reproduce the experimental results more quantitatively. As shown in Fig. 8, we obtain good agreement with experiments by employing the SEM-measured gate-wire spacings of $d_{BG} - 2a = 0.25 \mu\text{m}$ and $d_{SG} - 2a = 0.6 \mu\text{m}$ and $d_{\text{offset}} = 0.1 \mu\text{m}$. We use parameter values of $\varphi \sim 41.5^\circ$ and 131.5° for low- f and high- f modes, respectively, and $g = 0.0017$. The coupling strength should be compared to the value of $g \sim 0.0005$ calculated by the material parameters $l_{\text{eff}} = 4 \mu\text{m}$ and NW diameter of $0.4 \mu\text{m}$. The discrepancy is reasonable if we consider the shape of the gate electrodes, which have a flat plate geometry in the real device with a larger capacitance than that of the cylindrical shape used in the model calculation.

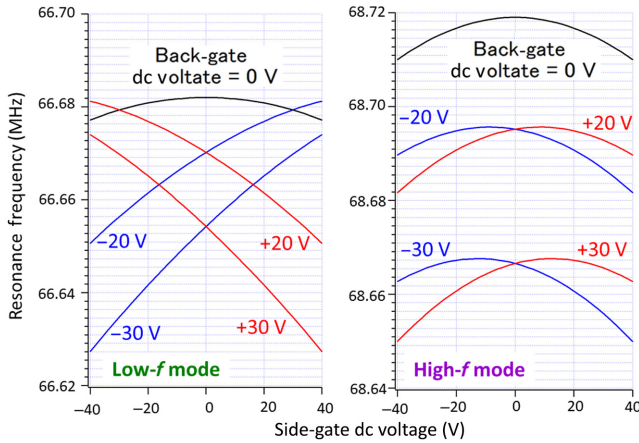


FIG. 8. Resonance frequency calculated using three-wire-capacitor model as a function of side- and back-gate voltages. Diameter ($2a$) of both the NW and electrode is assumed to be 400 nm . In the calculation, we use gate-wire spacing of $d_{BG} - 2a = 0.25 \mu\text{m}$ and $d_{SG} - 2a = 0.6 \mu\text{m}$ and $d_{\text{offset}} = 0.1 \mu\text{m}$, which are values obtained by SEM observation, with a low- f (high- f) mode tilt angle of 41.5° (131.5°) and coupling constant $g = 0.0017$.

The opposite double-gate response observed in the two nearly degenerate fundamental modes allows vectorial-frequency control, where two appropriately chosen gate voltages can independently modulate two frequencies. When the frequency shift induced by the gate voltage is small enough compared to frequency splitting between the two modes, we can apply the lowest-order approximation to the gate-voltage dependences given by

$$\begin{aligned}\Delta f_l(\vec{V}) &\equiv f_l(\vec{V}) - f_l[\vec{V} = (0, 0)] \\ &= \alpha_l V_{\text{dcBG}}^2 + \beta_l V_{\text{dcBG}} V_{\text{dcSG}} + \gamma_l V_{\text{dcSG}}^2, \\ \Delta f_h(\vec{V}) &\equiv f_h(\vec{V}) - f_h[\vec{V} = (0, 0)] \\ &= \alpha_h V_{\text{dcBG}}^2 + \beta_h V_{\text{dcBG}} V_{\text{dcSG}} + \gamma_h V_{\text{dcSG}}^2.\end{aligned}\quad (11)$$

Here, $f_l(\vec{V})$ and $f_h(\vec{V})$ are the resonance frequencies of low- f and high- f modes at bias voltages $\vec{V} = (V_{\text{dcBG}}, V_{\text{dcSG}})$. $\alpha_{l/h}$, $\beta_{l/h}$, and $\gamma_{l/h}$ are voltage-independent constants, which can be experimentally determined. The opposite double-gate response of the two modes is reflected in the sign of parameter β , where β_l is negative and β_h is positive. By solving Eq. (11) for given $\Delta f_l(V)$ and $\Delta f_h(V)$ with respect to V_{dcBG} and V_{dcSG} , we can find the two gate voltages that induce the desired frequency shifts for the two modes.

Figure 9 shows examples of vectorial-frequency control. The red circles in Figs. 9(a)–9(d) show the two dc voltages applied to the two gates, and the red triangles in Figs. 9(e)–9(h) show the two experimentally obtained resonance frequencies corresponding to each set of voltages. In Figs. 9(e) and 9(f), only one of the high- f and low- f mode frequencies is shifted. With the single-gate geometry, the dc voltage applied to the gate induces a frequency shift to both modes, and this separate frequency control is not enabled. Furthermore, we can demonstrate fixed red-sideband and blue-sideband frequency modulations, where the same and opposite signs of shifts are induced, as shown in Figs. 9(g) and 9(h), respectively. The black dashed lines indicate the expected frequencies given by Eq. (4), showing their good agreement with experiments. These results demonstrate that the double-gate geometry enables the independent control of the two mode frequencies.

In our device, frequency splitting of 2 MHz is naturally formed. This can be caused by the anisotropic shape of the NW cross section or the effect of the doubly clamped geometry with deposited electrodes, which cannot be perfectly eliminated in real devices. By independently adjusting the two frequencies, we can control the splitting and average frequency to utilize the unique properties reported in nearly degenerate two-mode systems, which is promising for improving the performance of NW-based nanomechanical sensors. It should also be noted that the piezoresistive detection scheme dominant in the core-shell NW device makes the detection efficiency independent of

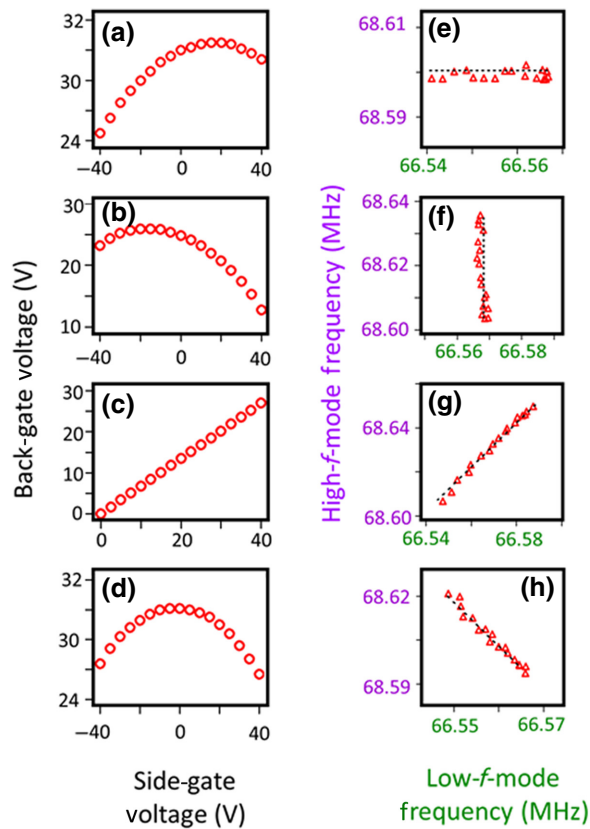


FIG. 9. (a)–(d) Sets of two gate voltages used for vector-frequency control. (e)–(h) Corresponding measured resonance frequencies. Low- f [high- f] mode frequency is changed using the sets of two voltages shown in (a) [(b)] with the high- f [low- f] mode frequency kept constant. Using the voltage sets shown in (c) [(d)], both frequencies are changed with their difference [sum] in (g) [(h)] maintained. Dashed black lines in (e)–(h) show values calculated using Eq. (11).

the gate voltage. This feature that detailed frequency tuning can be achieved without changing the transduction performance is important in realistic applications.

V. CONCLUSION

We study the mechanical vibrational properties of an InAs/GaP core-shell nanowire electromechanical resonator device with double-gate geometry. We confirm that the piezoresistance is the dominant mechanism in the vibration-induced conductance modulation, unlike in InAs nanowires, where the transconductance effect governs the modulation. Combined with a half-frequency drive technique, we can characterize the mechanical vibration properties without applying a dc gate voltage. We also study the shift in the resonance frequency of two nearly degenerate flexural modes as a function of the gate voltages applied to the double-gate electrodes. We find that the two modes have a different double-gate response, which

can be utilized to determine the vibration axis and for vector-frequency control.

ACKNOWLEDGMENT

This work is partly supported by JSPS KAKENHI (Grant No. JP21H01023).

- [1] N. P. Dasgupta, J. Sun, C. Liu, S. Brittman, S. C. Andrews, J. Lim, H. Gao, R. Yan, and P. Yang, 25th anniversary article: Semiconductor nanowires synthesis, characterization, and applications, *Adv. Mater.* **26**, 2137 (2014) and references therein.
- [2] A. N. Cleland, *Foundations of Nanomechanics: From Solid-State Theory to Device Applications* (Springer-Verlag, Berlin Heidelberg, 2003).
- [3] S. Schmid, L. G. Villanueva, and M. L. Roukes, *Fundamentals of Nanomechanical Resonators* (Springer International Publishing, Switzerland, 2016).
- [4] A. Husain, J. Hone, Henk W. Ch. Postma, X. M. H. Huang, T. Drake, M. Barbic, A. Scherer, and M. L. Roukes, Nanowire-based very-high-frequency electromechanical resonator, *Appl. Phys. Lett.* **83**, 1240 (2003).
- [5] A. Ayari, P. Vincent, S. Perisanu, M. Choueib, V. Goutenoire, M. Bechelany, D. Cornu, and S. T. Purcell, Self-oscillations in field emission nanowire mechanical resonators: A nanometric dc–ac conversion, *Nano Lett.* **7**, 2252 (2007).
- [6] R. He, X. L. Feng, M. L. Roukes, and P. Yang, Self-transducing silicon nanowire electromechanical systems at room temperature, *Nano Lett.* **8**, 1756 (2008).
- [7] H. S. Solanki, S. Sengupta, S. Dhara, V. Singh, S. Patil, R. Dhall, J. Parpia, A. Bhattacharya, and M. M. Deshmukh, Tuning mechanical modes and influence of charge screening in nanowire resonators, *Phys. Rev. B* **81**, 115459 (2010).
- [8] M. Sansa, M. Fernandez-Regulez, A. San Paulo, and F. Perez-Murano, Electrical transduction in nanomechanical resonators based on doubly clamped bottom-up silicon nanowires, *Appl. Phys. Lett.* **101**, 243115 (2012).
- [9] T. S. Abhilash, J. P. Mathew, S. Sengupta, M. R. Gokhale, A. Bhattacharya, and M. M. Deshmukh, Wide bandwidth nanowire electromechanics on insulating substrates at room temperature, *Nano Lett.* **12**, 6432 (2012).
- [10] C. B. Maliakkala, J. P. Mathew, N. Hatui, A. Azizur Rahman, M. M. Deshmukh, and A. Bhattacharya, Fabrication and characterization of GaN nanowire doubly clamped resonators, *J. Appl. Phys.* **118**, 114301 (2015).
- [11] J. P. Mathew, R. Patel, A. Borah, C. B. Maliakkal, T. S. Abhilash, and M. M. Deshmukh, Nanoscale electromechanics to measure thermal conductivity, expansion, and interfacial losses, *Nano Lett.* **15**, 7621 (2015).
- [12] H. S. Solanki, S. Sengupta, S. Dubey, V. Singh, S. Dhara, A. Kumar, A. Bhattacharya, S. Ramakrishnan, A. A. Clerks, and M. M. Deshmukh, High Q electromechanics with InAs nanowire quantum dots, *Appl. Phys. Lett.* **99**, 213104 (2011).

- [13] M. Montinaro, G. Wüst, M. Munsch, Y. Fontana, E. Russo-Averchi, M. Heiss, A. Fontcuberta i Morral, R. J. Warburton, and M. Poggio, Quantum dot opto-mechanics in a fully self-assembled nanowire, *Nano Lett.* **14**, 4454 (2014).
- [14] M. Kim, J. Kim, Y. Hou, D. Yu, Y.-J. Doh, B. Kim, K. W. Kim, and J. Suh, Nanomechanical characterization of quantum interference in a topological insulator nanowire, *Nat. Commun.* **10**, 4522 (2019).
- [15] B. Lassagne, Y. Tarakanov, J. Kinaret, D. Garcia-Sanchez, and A. Bachtold, Coupling mechanics to charge transport in carbon nanotube mechanical resonators, *Science* **325**, 1107 (2009).
- [16] G. A. Steele, A. K. Hüttel, B. Witkamp, M. Poot, H. B. Meerwaldt, L. P. Kouwenhoven, and H. S. J. van der Zant, Strong coupling between single-electron tunneling and nanomechanical motion, *Science* **325**, 1103 (2009).
- [17] E. Gil-Santos, D. Ramos, J. Martínez, M. Fernández-Regúlez, R. García, Á San Paulo, M. Calleja, and J. Tamayo, Nanomechanical mass sensing and stiffness spectrometry based on two-dimensional vibrations of resonant nanowires, *Nat. Nanotechnol.* **5**, 641 (2010).
- [18] D. Cadeddu, F. R. Braakman, G. Tütüncüoğlu, F. Matteini, D. Ruffer, A. Fontcuberta i Morral, and M. Poggio, Time-resolved nonlinear coupling between orthogonal flexural modes of a pristine GaAs nanowire, *Nano Lett.* **16**, 926 (2016).
- [19] A. P. Foster, J. K. Maguire, J. P. Bradley, T. P. Lyons, A. B. Krysa, A. M. Fox, M. S. Skolnick, and L. R. Wilson, Tuning nonlinear mechanical mode coupling in GaAs nanowires using cross-section morphology control, *Nano Lett.* **16**, 7414 (2016).
- [20] J. P. Mathewa, A. Bhushanb, and M. M. Deshmukh, Tension mediated nonlinear coupling between orthogonal mechanical modes of nanowire resonators, *Solid State Commun.* **282**, 17 (2018).
- [21] L. M. de Lépinay, B. Pigeau, B. Besga, P. Vincent, P. Poncharal, and O. Arcizet, A universal and ultrasensitive vectorial nanomechanical sensor for imaging 2D force fields, *Nat. Nanotechnol.* **12**, 156 (2017).
- [22] N. Rossi, F. R. Braakman, D. Cadeddu, D. Vasyukov, G. Tütüncüoğlu, A. Fontcuberta i Morral, and M. Poggio, Vectorial scanning force microscopy using a nanowire sensor, *Nat. Nanotechnol.* **12**, 150 (2017).
- [23] F. R. Braakman, N. Rossi, G. Tütüncüoğlu, A. Fontcuberta i Morral, and Martino Poggio, Coherent Two-Mode Dynamics of a Nanowire Force Sensor, *Phys. Rev. Appl.* **9**, 054045 (2018).
- [24] J. Rieger, T. Faust, M. J. Seitner, J. P. Kotthaus, and E. M. Weig, Frequency and Q-factor control of nanomechanical resonators, *Appl. Phys. Lett.* **101**, 103110 (2012).
- [25] T. Faust, J. Rieger, M. J. Seitner, J. P. Kotthaus, and E. M. Weig, Coherent control of a classical nanomechanical two-level system, *Nat. Phys.* **9**, 485 (2013).
- [26] A. Benyamini, A. Hamo, S. V. Kusminskiy, F. von Oppen, and S. Ilani, Real-space tailoring of the electron-phonon coupling in ultraclean nanotube mechanical resonators, *Nat. Phys.* **10**, 151 (2014).
- [27] I. Khivrich, A. A. Clerk, and S. Ilani, Nanomechanical pump-probe measurements of insulating electronic states in a carbon nanotube, *Nat. Nanotechnol.* **14**, 161 (2019).
- [28] J. M. Nichol, E. R. Hemesath, L. J. Lauhon, and R. Budakian, Displacement detection of silicon nanowires by polarization-enhanced fiber-optic interferometry, *Appl. Phys. Lett.* **93**, 193110 (2008).
- [29] E. Gil-Santos, D. Ramos, V. Pini, J. Llorens, M. Fernández-Regúlez, M. Calleja, J. Tamayo, and A. San Paulo, Optical back-action in silicon nanowire resonators: Bolometric versus radiation pressure effects, *New J. Phys.* **15**, 035001 (2013).
- [30] H. Okamoto, N. Kitajima, K. Onomitsu, R. Kometani, S. Warisawa, S. Ishihara, and H. Yamaguchi, High-sensitivity charge detection using antisymmetric vibration in coupled micromechanical oscillators, *Appl. Phys. Lett.* **98**, 014103 (2011).
- [31] H. Okamoto, A. Gourgout, C.-Y. Chang, K. Onomitsu, I. Mahboob, E. Y. Chang, and H. Yamaguchi, Coherent phonon manipulation in coupled mechanical resonators, *Nat. Phys.* **9**, 480 (2013).
- [32] X. Mao, G.-Q. Qin, H. Yang, H. Zhang, M. Wang, and G.-L. Long, Enhanced sensitivity of optical gyroscope in a mechanical parity-time-symmetric system based on exceptional point, *New J. Phys.* **22**, 093009 (2020).
- [33] O. Malvar, E. Gil-Santos, J. J. Ruz, D. Ramos, V. Pini, M. Fernandez-Regulez, M. Calleja, J. Tamayo, and A. San Paulo, Tapered silicon nanowires for enhanced nanomechanical sensing, *Appl. Phys. Lett.* **103**, 033101 (2013).
- [34] See the Supplemental Material at <http://link.aps.org/supplemental/10.1103/PhysRevApplied.17.044042> for gated transport characteristics, detailed calculation of the resonance frequency for a tapered beam, measurements on Duffing bistability, and derivation of the elastance matrix.
- [35] W. Tomita, S. Sasaki, K. Tateno, H. Okamoto, and H. Yamaguchi, *Phys. Status Solidi B* **257**, 1900401 (2019).
- [36] V. Sazonova, Y. Yaish, H. Ustunel, D. Roundy, T. A. Arias, and P. L. McEuen, A tunable carbon nanotube electromechanical oscillator, *Nature* **431**, 284 (2004).
- [37] B. Lassagne, D. Garcia-Sanchez, A. Aguasca, and A. Bachtold, *Nano Lett.* **8**, 3735 (2008).
- [38] A. N. Cleland, J. S. Aldridge, D. C. Driscoll, and A. C. Gossard, Nanomechanical displacement sensing using a quantum point contact, *Appl. Phys. Lett.* **81**, 1699 (2002).
- [39] D. Ruger and P. Grutter, Mechanical Parametric Amplification and Thermomechanical Noise Squeezing, *Phys. Rev. Lett.* **67**, 699 (1991).
- [40] M. Keplinger, T. Mårtensson, J. Stangl, E. Wintersberger, B. Mandl, D. Kriegner, V. Holy, G. Bauer, K. Deppert, and L. Samuelson, Structural investigations of core-shell nanowires using grazing incidence X-ray diffraction, *Nano Lett.* **9**, 1877 (2009).
- [41] See for example, D. H. Trevena, *Static Fields in Electricity and Magnetism* (Butterworths, London, 1961).